Geophys. J. Int. (1995) **120**, 145–162

P-wave array polarization analysis and effective anisotropy of the brittle crust

Götz H. R. Bokelmann
Institute of Geophysics, Ruhr-University Bochum, D-44780 Bochum, Germany

Accepted 1994 July 8. Received 1994 April 5; in original form 1993 November 18.

SUMMARY

P-wave polarization constrains local anisotropy in the vicinity of the receivers. Using three-component and array data from the regional GERESS array in south-eastern Germany, we measure polarization **a** and propagation vectors **s** for *P* phases of 120 events. Angular deviations **a**–**s** between these normalized vectors often approach 10°, rendering them easily measurable. The effect of anisotropy can be distinguished from remote effects, since all remote effects, such as source mislocation, distant lateral heterogeneity or distant anisotropy, affect polarization and propagation vectors simultaneously. Averaging removes sensitivity to near-receiver heterogeneity, and local anisotropy is left as the sole cause of the effects in **a**–**s**. This method hence gives local effective anisotropy in the near-receiver crust averaging over a depth interval of a wavelength (≈6 km). We resolve strike and dip of the symmetry plane and also two dimensionless numbers η and τ which give constraints on four of the elastic parameters. The optimum model (variance reduction 44 per cent) has symmetry plane orientation of strike 113° and dip 49° to the north, which corresponds closely to the consistently observed gneiss foliation direction in the area (120°, 50°–60°). Comparing η and τ with predictions from different physical models we find that the data are fit by a gneiss model assuming that the anisotropy is dominated by the mica, if 3–8 per cent of the mica are well aligned. This suggests that anisotropy in the region studied is dominated by the effect of local foliation rather than the regional stress field.

Key words: anisotropy, array seismology, inversion, polarization, wave propagation.

1 INTRODUCTION

In a pioneering study of anisotropy in the Earth, Hess (1964) showed that azimuthal traveltime delays of oceanic P_n can be explained by aligned olivine crystals in the oceanic upper mantle. For such a phase, which travels subhorizontally on most of its path, Backus (1965) showed that azimuthal traveltime variation is characterized by a rather simple trigonometric expression, given that anisotropy is weak. Fitting of such trigonometric terms has subsequently been used for teleseismic *P* waves, e.g. in Dziewonski & Anderson (1983). Interpretation of such data, however, is complicated by the fact that lateral heterogeneity can also cause azimuthal variation. This trade-off is often difficult to resolve from traveltime data alone. The second type of 'classical' anisotropy study is shear-wave splitting (Ando, Ishikawa & Yamazaki 1983; Silver & Chan 1991), a technique which uses the strong effect of anisotropy on waveforms of shear waves due to different speeds of the two orthogonally polarized shear waves. The constraint on anisotropy is not unlike that of traveltimes. Both give integral constraints only, namely on bulk anisotropy along the wave path. Hence, for both methods a trade-off exists between size of anisotropy and extent of anisotropic path. More importantly, an anisotropic region is difficult to localize using these data. For example, mantle anisotropy can be inferred from shear-wave splitting data only if the observed effects are too large to be explained by crustal anisotropy alone. This is somewhat unsatisfying, and methods for independent determination of anisotropy in the crust under the receivers should be sought. This paper, in fact, demonstrates that (beside active experiments) an entirely independent constraint on near-receiver anisotropy is possible, which follows from analysis of three-component array data.

Anisotropy studies using traveltimes and shear-wave splitting can be performed with single-station data, in the latter case requiring a three-component instrument. For the

present study of P-wave phases, we use array and three-component data from the GERESS array. These array data allow determination of the propagation vector $\mathbf{s} = \mathbf{k}/\omega$ of plane waves crossing the array. While this particular feature of beam-forming is well appreciated for signal enhancement, event detection and localization (Beauchamp 1975), this particular strength has apparently not been used in anisotropy studies so far.

The propagation vector, given by $\mathbf{s} = \nabla t$, may be specified by azimuth θ_s and horizontal slowness $p = \sqrt{s_x^2 + s_y^2}$ or alternatively by incidence angle $\phi_s = \sin^{-1}(pv)$ with the local velocity v. On the other hand, three-component stations allow determination of the polarization vector $\mathbf{a}$, which gives the dominant direction of linear particle motion. $\mathbf{a}$ can be specified by azimuth θ_a and incidence angle ϕ_a. In the following we restrict our attention to normalized $\mathbf{s}$ and $\mathbf{a}$, namely to azimuth and incidence angles. This effectively ignores that the array also gives estimates of the apparent velocity. Neither of the two azimuth estimates θ_s and θ_a necessarily corresponds to the azimuth of the receiver–source great circle, since heterogeneity, anisotropy and other effects may cause deviations. The same is true for the incidence angles. For a known source location we get predictions (θ_p, ϕ_p) for a reference earth model. Comparing (θ_s, ϕ_s) and (θ_a, ϕ_a) with the predictions gives rise to so-called mislocation diagrams.

For the purpose of event localization the two data types and correspondingly their mislocation patterns are typically treated the same, where the azimuth is used for localization purposes, while the incidence angle serves for identification of the phase type for regional events and of epicentral distance in the case of teleseismic events. Interestingly, source location procedures have so far disregarded that these two observed quantities, namely propagation and polarization vectors, are principally different. While they coincide in an isotropic earth, elastic anisotropy would affect propagation and polarization vectors differently. For event localization, this means that there is a systematic bias between propagation and polarization vectors, which should be removed by taking local anisotropy into account. This systematic bias, however, is the prime quantity of interest in this study, since it offers us a new constraint on anisotropy in the vicinity of the receivers (in fact exclusively there). In this study we use only polarization and propagation vectors. Traveltime and amplitude information is not used, since this might obscure the near-receiver crustal anisotropy with information gathered somewhere along the ray paths.

2 OBSERVATIONS

2.1 GERESS array

The GERman Experimental Seismic System GERESS (Harjes 1990), shown in Fig. 1, is a regional seismological array with an aperture of about 4 km consisting of 25 stations with 1 Hz vertical short-period instruments (Geotech GS-13) sampled at 40 Hz, with four of them also equipped with horizontal components (A2, D1, D4, D7; triangles). Additional three-component instruments at the C2 location are sampled at 120 Hz (Geotech GS-13) and 10 Hz (Geotech BB-13). For further descriptions of installation criteria, performance and operation see Harjes (1990) and Harjes *et al.* (1983). The array is located in eastern Bavaria, Germany, in a hilly region on crystalline outcrop of the Bohemian massive, with topographic variation of about 200 m across the array. A major advantage of data from the GERESS array is that there are no sediments under the stations, greatly improving the quality, particularly of the polarization data. Otherwise P–S conversions at the crust–sediment boundary might perhaps disturb polarizations substantially.

2.2 Events

This study uses a set of 95 events recorded at GERESS array stations in the time interval between 1990 May and 1993 January (Table 1), which comprise the whole range from regional to teleseismic distance. The emphasis in this study is on first-arriving phases. The only later arriving phase is *PcP*, in three cases. The chosen events in Table 1 are part of a larger set of events. For several events either the polarization or propagation vector had to be discarded, particularly early on in the experiment. In general, events were discarded if data from less than three three-component stations or nine array stations were available. Out of 112 events with acceptable polarization data, 81 had data for all six three-component instruments present. Out of 108 events with acceptable propagation data, 88 had data from at least 20 array stations.

2.3 Determination of polarization directions

Now we discuss procedures of extracting backazimuth and incidence angle information from three-component and array data. For three-component data $\mathbf{u}^j = (u_i)^j$ with components $j = 1, 2, 3$, the covariance matrix at zero-lag is computed as

$$S_{jk} = \frac{1}{N} \sum_{i=1}^{N} u_i^j u_i^k, \tag{1}$$

where N is the number of samples in the time window. Obviously, $\mathbf{S}$ is symmetrical, so that its eigenvalues λ^j are real and non-negative. We choose a set of three orthonormal eigenvectors $\mathbf{a}^j$. $\lambda^j \mathbf{a}^j$ (no summation) then give the axis of the polarization ellipsoid (see, for example, Kanasewich 1981). If the particle motion is linearly polarized, then $\lambda^2 = \lambda^3 = 0$. For elliptical particle motion (within a polarization plane), we have $\lambda^3 = 0$. In general, however, the particle motion is ellipsoidal due to the presence of noise. If we take components (1, 2, 3) as (vertical up, north, east), the incidence angle is $\phi_a = \cos^{-1}|u_1^1|$ and the backazimuth is

$$\theta_a = \begin{cases} \tan^{-1}\left(\dfrac{a_3^1}{a_2^1}\right) & \text{for } a_1^1 < 0 \\ \pi + \tan^{-1}\left(\dfrac{a_3^1}{a_2^1}\right) & \text{for } a_1^1 \geq 0 \end{cases}.$$

A simple check of the quality of the measurement is given by the rectilinearity

$$1 - \frac{\lambda^2 + \lambda^3}{2\lambda^1}, \tag{2}$$

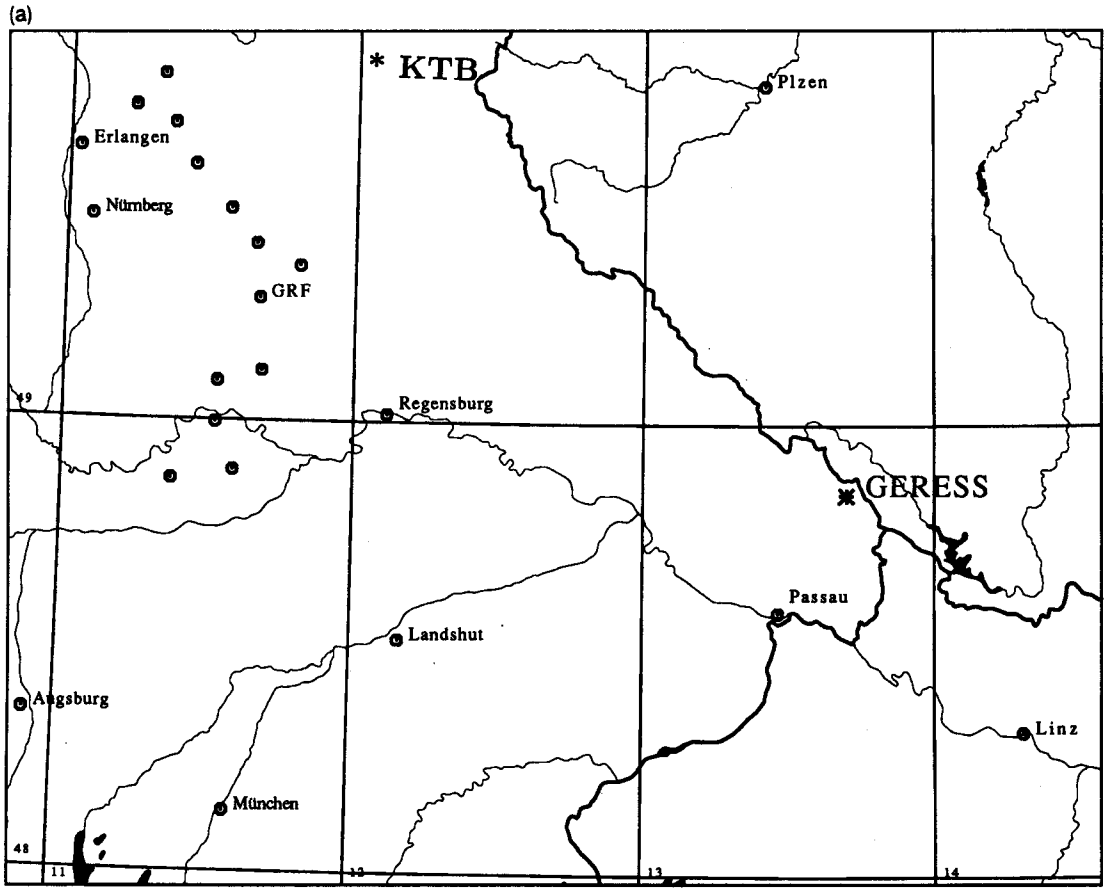

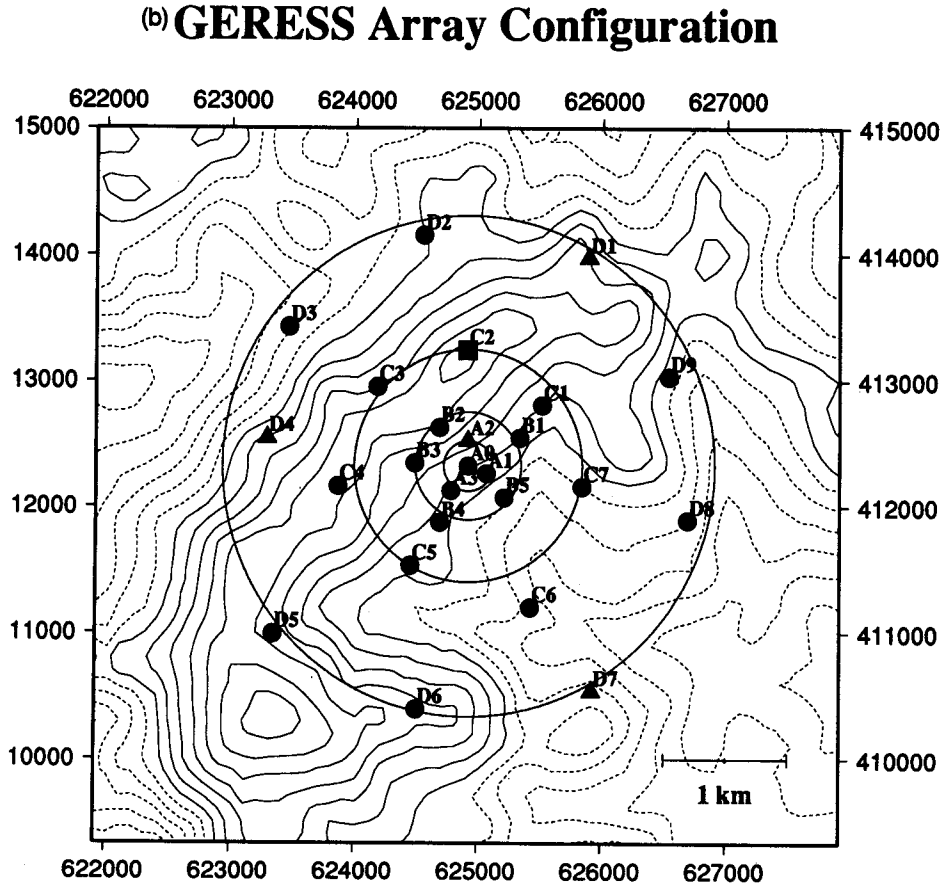

Figure 1. (a) Geographic location of the GERESS array in south-eastern Germany. Borders with Austria and the Czech Republic are shown by thick lines. (b) Array locations in Gauss–Krüger coordinates. Data from 25 vertical-component short-period instruments and three-component instruments (triangles and rectangles) are used in this paper. The topographic variation across the array is about 200 m.

Table 1. Events used in this study.
(Location and time from PDE Monthly Bulletin, if not stated otherwise.)

Year, Day, Hour, Min, Sec.	Latitude	Longitude	Depth	Phase
1990 123 01 03 38	43.315	19.890	5.	Pn
1990 240 20 21 22	36.267	27.218	39.9	Pn
1990 246 10 48 33	45.915	15.873	20.	Pn
1990 253 12 17 36	70.770	-13.803	10.	P
1990 258 23 07 43	64.655	-17.617	10.	P
1990 285 17 30 00	37.250	-116.490	0.	P
1990 297 15 04 14	73.360	54.670	0.	P
1990 318 18 11 58	-22.258	-138.805	0.	PKP
1990 325 16 59 58	-21.9	-138.980	0.	PKP
1990 331 04 37 58	43.853	16.633	24.	Pn
1990 331 04 51 36	43.895	16.641	10.	Pn
1990 347 00 24 26	37.3	15.438	11.1	Pn
1990 348 03 21 27	39.347	15.355	276.	Pn
1990 350 15 45 41	41.361	43.715	33.	P
1990 355 13 12 53	-18.891	-177.971	457.	PKP
1991 038 07 12 48	47.590	15.503	10.	Pn
1991 042 15 43 44	44.871	6.704	14.	Pn
1991 059 15 29 42	51.690	16.360	0.	Pn
1991 074 03 24 09	34.343	26.389	7.1	Pn
1991 078 02 51 26	39.260	20.429	10.	Pn
1991 094 19 00 00	37.296	-116.313	0.	P,PcP
1991 100 01 08 40	37.359	36.221	10.	P
1991 111 08 51 56	37.972	19.952	39.8	Pn
1991 116 22 35 11	43.446	16.244	12.	Pn
1991 119 09 12 48	42.453	43.673	17.2	P
1991 119 18 30 42	42.503	43.899	14.3	P
1991 120 03 40 36	51.690	16.206	10.	Pn
1991 122 10 15 17	47.929	16.209	10.	Pn
1991 123 23 41 02	42.647	43.263	10.8	P
1991 136 02 06 17	52.309	7.649	52.4	Pn
1991 138 17 14 59	-21.832	-139.014	0.	PKP
1991 143 19 42 56	51.416	15.850	10.	Pn
1991 149 18 59 58	-22.256	-138.794	0.	PKP
1991 149 20 24 40	45.016	8.213	10.	Pn
1991 154 10 22 40	40.048	42.859	27.8	P
1991 165 17 59 58	-21.944	-138.988	0.	PKP
1991 166 00 59 20	42.461	44.009	9.4	P
1991 185 06 26 32	42.387	44.116	20.4	P
1991 191 23 57 20	51.424	16.217	0.	Pn
1991 196 18 09 58	-21.877	-138.963	0.	PKP
1991 200 01 19 52	45.344	21.123	10.	Pn
1991 200 01 27 32	45.312	21.053	10.	Pn
1991 222 05 23 48	51.428	16.242	0.	Pn
1991 252 18 36 52	51.414	16.220	0.	Pn
1991 257 19 00 00	37.226	-116.428	0.	P,PcP
1991 279 01 46 48	41.096	43.409	18.3	P
1991 281 03 31 16	45.587	149.049	146.	P
1991 291 19 12 00	37.063	-116.045	0.	P,PcP
1991 301 00 21 32	44.265	21.456	67.	Pn
1991 303 16 24 21	45.029	9.937	10.7	Pn
1991 304 09 31 17	45.011	10.059	10.	Pn
1991 324 01 54 17	46.778	9.519	10.	Pn
1991 325 02 16 32	45.491	21.176	27.	Pn
1991 326 07 40 01	45.019	9.985	11.	Pn
1991 327 01 06 31	51.428	16.243	0.	Pn
1991 332 17 19 56	36.924	49.603	15.7	P
1991 336 08 49 40	45.498	21.115	9.	Pn
1991 336 09 04 43	45.437	21.247	10.	Pn
1991 337 16 58 23	44.994	9.965	14.	Pn
1991 338 13 31 31	44.978	9.932	19.6	Pn
1991 351 06 38 17	47.393	151.499	157.	P
1991 353 03 12 22	45.907	21.569	10.	Pn
1991 353 18 55 17	28.102	57.304	27.	P
1991 354 02 06 05	24.720	93.103	41.	P
1991 356 08 43 13	45.533	151.021	25.	P
1992 001 10 12 20	44.984	9.962	23.1	Pn
1992 002 19 41 45	5.638	-73.832	134.	P
1992 014 12 22 22	51.534	16.181	10.	Pn
1992 023 06 27 39	38.356	20.307	10.	Pn
1992 033 00 31 30	-51.547	139.704	10.	PKP
1992 048 00 01 57	79.191	124.482	10.	P
1992 048 19 23 14	46.761	9.505	10.	Pn
1992 052 20 50 32	45.463	14.328	11.	Pn
1992 062 12 29 40	52.915	159.886	39.	P
1992 065 14 39 10	52.9	159.619	45.	P
1992 067 01 53 38	10.210	-84.323	79.	P
1992 073 17 18 43	40.2	39.500	27.2	P
1992 103 08 19 30	43.964	13.022	10.	Pn
1992 104 01 20 01	51.157	5.815	15.	Pn
1992 112 22 28 06	43.264	17.961	33.	Pn
1992 126 16 48 03	43.286	17.471	10.	Pn
1992 129 06 44 39	47.248	9.584	10.	Pn
1992 129 07 51 25	47.233	9.564	10.	Pn
1992 130 05 37 58	49.953	7.409	10.	Pn
1992 136 00 43 42	47.239	9.543	5.	Pn
1992 140 14 25 04	49.105	6.623	18.	Pn
1992 142 04 59 57	41.591	88.805	0.	P
1992 148 18 14 00	44.406	11.737	10.	Pn
1992 149 09 52 42*	44.150	11.466	5.	Pn
1992 149 12 26 02*	43.966	11.977	13.6	Pn
1992 286 13 09 56	29.888	31.223	24.7	P
1992 297 23 19 47	42.503	45.073	33.	P
1992 323 21 10 41	38.300	22.428	10.	Pn
1992 326 05 07 23	35.931	22.443	70.2	P
1993 027 23 41 00	35.963	22.511	62.8	Pn

* Location and time information from the Istituto Nazionale di Geofisica, Italy.

which is equal to 1 for linear polarization and 0 in the worst case of 'spherical' polarization, when all eigenvalues have the same size.

Figure 2 shows a seismogram example demonstrating a few characteristics of the eigenvector analysis. For this data example (year 1992 day 48 hour 19) with an epicentral distance of 385 km and backazimuth of 235° a number of regional phases are visible. The main phases for this distance range are P_n, P_g, S_n and S_g. They are visible in the three-component seismogram on the top. The lower traces give polarization attributes computed using a gliding window with a length of 2 s: the rms amplitude of the three-component seismogram or 'three-component size' (fourth trace) $\sqrt{\sum_j \lambda^j} = \sqrt{\sum_j S_{jj}}$ shows P_g, S_n and S_g clearly. The first-arriving P_n shows up with somewhat smaller three-component size, but with the highest rectilinearity (2), with close-to-ideal linear polarization. A line gives the critical rectilinearity level of 0.9. Only P_n and P_g exceed this level. Since the eigenvalues are related to energy, error bars can be obtained from the F-test (see Bokelmann 1992). S_g shows up with higher rectilinearity than other S phases and also with substantial three-component size. The horizontal–vertical ratio $(H/V)\sqrt{S_2 + S_3/S_1}$ and similarly the radial–transverse ratio (R/T) computed from the elements of the covariance matrix are also indicative of the phase character. Values of $H/V = 1$ and $R/T = 1$ are shown by lines

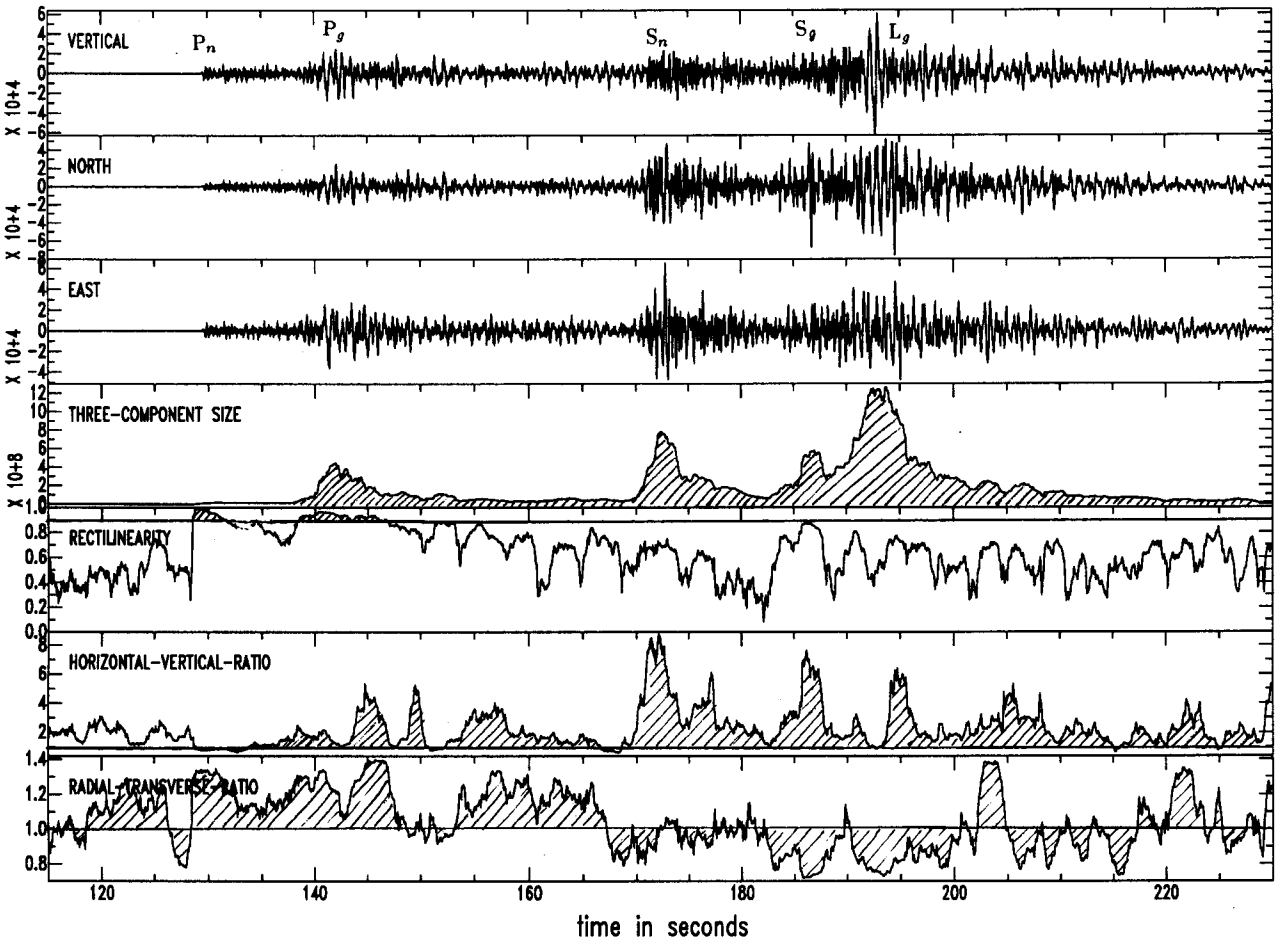

Figure 2. Polarization attributes for three-component data indicative of body-wave phases. The three-component amplitude and the rms amplitude of the three-component seismogram show the main phases clearly. Rectilinearity and component ratios allow determination of the wave type.

indicating polarization angles near 45°. For the *S*-phase train H/V shows very clear horizontally polarized phases S_n, S_g and L_g, which also show small values of R/T. This radial–transverse ratio for *P* phases shows clearly radially polarized energy. In summary, polarization is an important tool for phase identification.

In the following we want to use polarization data for the set of *P* and *PcP* phases. For these phases, polarization attributes are slowly varying (Fig. 2). In fact, they are also rather insensitive to the particular choice of window length. On the six three-component stations we observe for P_n a backazimuth of $\theta_a = 240.4° \pm 5.5°$ and an incidence angle of $\phi_a = 44.9° \pm 4.2°$. These angle estimates correspond closely to values extracted manually from hodograms and are near predicted values from the IASP91 earth model and source locations from Table 1 ($\theta_p = 235.17°$ and $\phi_p = 40.02°$).

Typically, we have data from six three-component stations available. Computing standard errors from the empirical distribution of these values, the average uncertainty is 3.5° for the incidence angle and 4.9° for the backazimuth. These are values, which may be seen as typical for events with high signal-to-noise ratio.

A slightly different approach was taken by Jurkewicz (1988), who proposed averaging covariance matrices of individual three-component stations before performing the eigenvector analysis to stabilize the estimates. In any case, polarization analysis lends itself to very efficient semi-automatic processing. Caution is required, however, for phases closely spaced in time, particularly if their amplitudes differ substantially. For regional phases this case is not uncommon. Window lengths in this study are allowed to vary depending on data type and quality. The median window length is near 3.5 s. Similarly, corner frequencies of a zero-phase bandpass filter were allowed to vary within 0.6–4 Hz to adapt to the different wave types.

2.4 The mislocation hemisphere

Figure 3 shows part of the lower hemisphere (0°–50°) of polarization anomalies, namely deviations of observed polarization from predicted polarization, where predicted again refers to values computed from the IASP91 model with source locations from Table 1. Here the free-surface effect is taken into account, as will be discussed below. In such a display, the centre corresponds to vertical incidence; the perimeter gives 50° incidence with north at the top. We choose this type of diagram to facilitate comparison with predicted polarization patterns from anisotropic models.

Multiple nuclear events from two source regions (Nevada, Tuamotu) give rather consistent deviations of polarization to

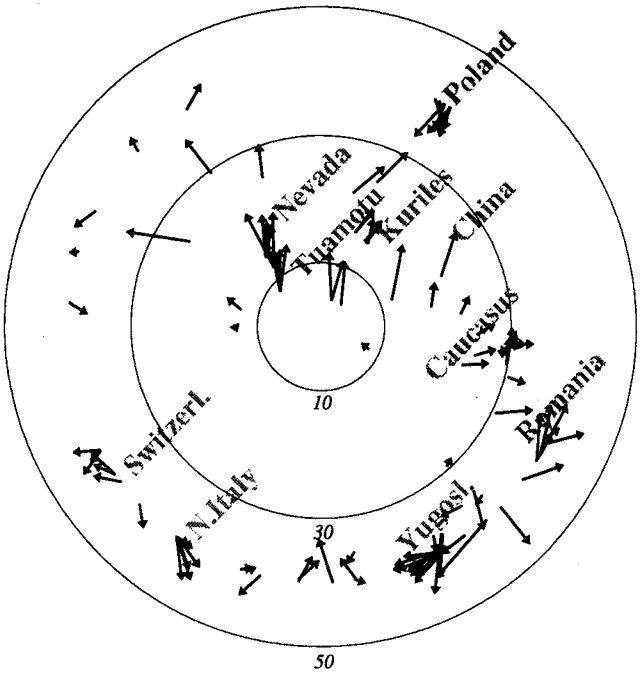

Figure 3. Lower hemisphere under the GERESS array (to 50° incidence) showing event polarization anomalies averaged over all three-component instruments. In this display (and the following ones), north is up. Lower hemisphere locations of first-arriving phases for a few geographical regions are shown. Note the consistent deviation to northern directions for phases steeply incident from the north.

more northern directions. Also other geographic regions with several nearby events give rise to consistent polarization effects. For steeply incident phases from the north there is a general deviation to more northern directions, while the southern part of Fig. 3 shows tangential deviations, apparently varying rapidly over the lower hemisphere. For example, polarization anomalies from northern Italy and Switzerland show opposite tangential effects. However, based on polarization data alone, this behaviour can not be interpreted in terms of heterogeneity or anisotropy. Consistently occurring source mislocation effects for these regional distances might also cause such variation. While this may be a problem of either polarization vector data or propagation vector data taken by itself, the difference is insensitive to source location errors and also to distant lateral heterogeneity. Instrument calibrations were performed daily. Substantial deviations from the nominal response were rare and the correction had a rather small effect on the lower hemisphere representation.

2.5 Free surface

Conversion at the free surface perturbs the incidence angle of the polarization direction. The apparent incidence angle ϕ_a' for a P wave is given by

$$\phi_a' = \tan^{-1}\left[\frac{2\sin(\phi_a)\sqrt{A^2-\sin^2(\phi_a)}}{A^2-2\sin^2(\phi_a)}\right]. \quad (3)$$

with the velocity ratio $A = v_p/v_s$ (Aki & Richards 1983). The dependence of ϕ_a' on ϕ is shown in Fig. 4 for a number

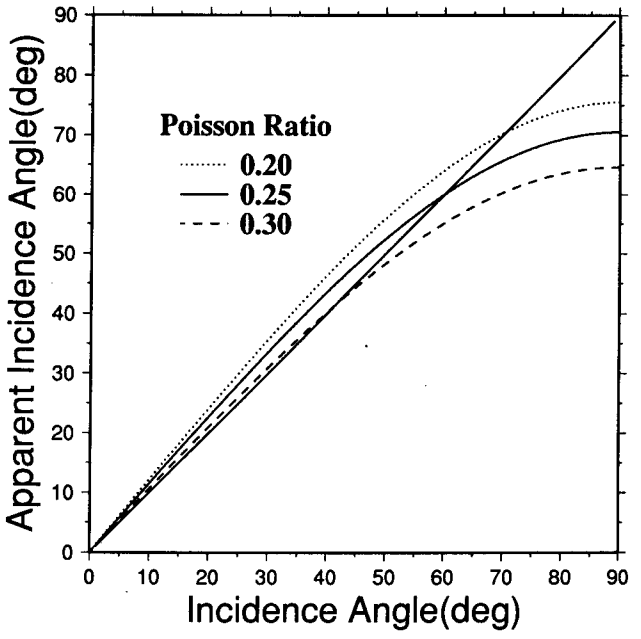

Figure 4. Free-surface effect on polarization incidence angles for a set of Poisson ratios.

of Poisson's ratios κ, which are related to the velocity ratio A by $\kappa = (A^{-2}-0.5)/(A^{-2}-1)$. The three values are $\kappa = 0.2$ ($A = 1.63$; dotted line), $\kappa = 0.25$ ($A = 1.73$; solid line) and $\kappa = 0.3$ ($A = 1.87$; broken line). Fig. 4 shows that the free-surface effect causes incidence angle deviations of several degrees. The free-surface correction is particularly important for large incidence angles. Variation of κ from $\kappa = 0.25$ by 0.05 produces offsets within 5° in the incidence range of our study (4°–40°). The deviation between the curves is within a few degrees. For the free-surface correction (Fig. 3) we used a crustal Poisson ratio of $\kappa = 0.25$. This corresponds closely to the upper crustal mean value observed in the KTB drill hole, which is located about 150 km north-west (Fig. 1a) in a similar crystalline geological setting (Fig. 1). Without this correction, the lower hemisphere has a distinctly different appearance (Fig. 5) with a clear radial component. The mean of this radial component is 5.1° oriented outwards. Clearly, the free-surface correction is an important and observable effect, which must be taken into account. On the other hand, we have seen that there are clear effects in Fig. 3 beyond the simple effect of crustal Poisson ratio alone. For the southern part of Fig. 3 the radial effect almost vanishes.

2.6 Array measurements

Propagation directions (θ_s, ϕ_s) can be extracted from array data either from traveltimes or from fk-analysis. Characteristics of this problem have been studied by Bokelmann (1993), where it was shown that small-array data like the ones in this paper can produce propagation vector data with reasonable uncertainty, given that topography (Fig. 1) is taken into account. We obtain the mislocation pattern of Fig. 6. Conversion from slowness p to incidence angle $\phi_a = \sin^{-1}(pv)$ was done using the local velocity estimate of $v = 5.2\,\mathrm{km\,s^{-1}}$ obtained from 3-D array analysis (Bokel-

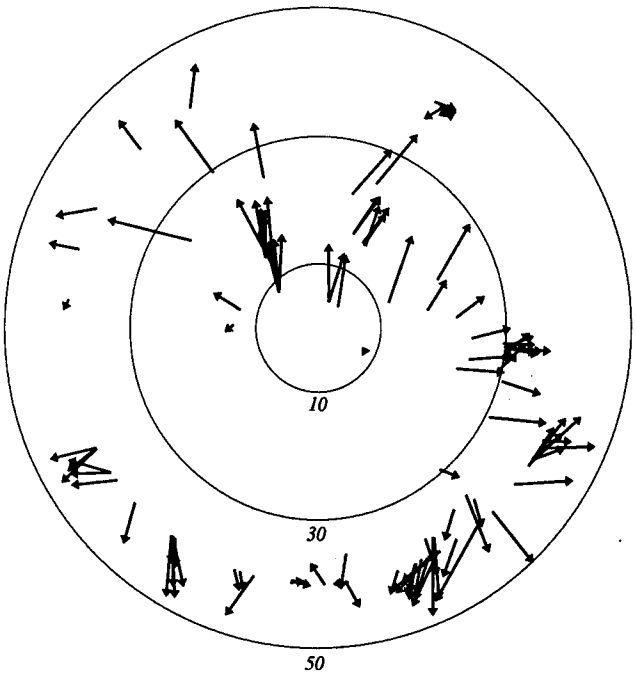

Figure 5. Lower hemisphere representation of polarization anomalies (without free-surface correction). Compared with Fig. 3 there is a clear radial component with a mean of 5.1°. Clearly, the free-surface effect gives rise to an observable effect which must be corrected.

mann 1993). In that paper, Nevada and Tuamotu nuclear events were studied. These show comparatively small deviation in Fig. 6. Nevertheless, these deviations turned out to be statistically significant (Bokelmann 1993). There are even larger anomalies in the data though. The northern deviation for steeply incident phases from the north, which was observed for polarization data (Fig. 3), is not apparent in the array data. Interestingly the patterns for Yugoslavia and Romania are very similar to observed polarization anomalies in Fig. 3 as well as the rapid variation of Switzerland and northern Italy. This suggests that either lateral heterogeneity or source mislocation is affecting propagation and polarization directions.

For an epicentral distance of about 400 km the mean tangential deviation between Switzerland and northern Italian events would require a relative source mislocation of about 70 km occurring consistently in the PDE solutions (Preliminary Determination of Epicenters, Monthly Listing, US Geological Survey) between the two source regions. While this is not impossible, lateral heterogeneity, the Alpine root, might also cause the azimuthal deviation, or respectively, a source mislocation in the PDE Bulletin (Table 1). Both would simultaneously perturb propagation and polarization directions.

Nevertheless, the procedure of relative analysis of polarization and propagation data gives data which are independent of the source location and distance lateral heterogeneity. The relative data (polarization–propagation vectors) from the 95 events are shown in Fig. 7. Nevada, Tuamotu, and other regions still show up with consistent effects. Naturally, the random scatter is larger for these differences than for the individual data. For two events the difference data were clearly dominated by noise and had to be removed. It may seem surprising that source mislocation and distant heterogeneity do not affect the relative data. This can be explained by the fact that the method does not require knowledge of source locations at all. While the propagation vector is used to determine the location in the lower hemisphere, the polarization vector deviation indicates the presence of anisotropy. This allows the study of

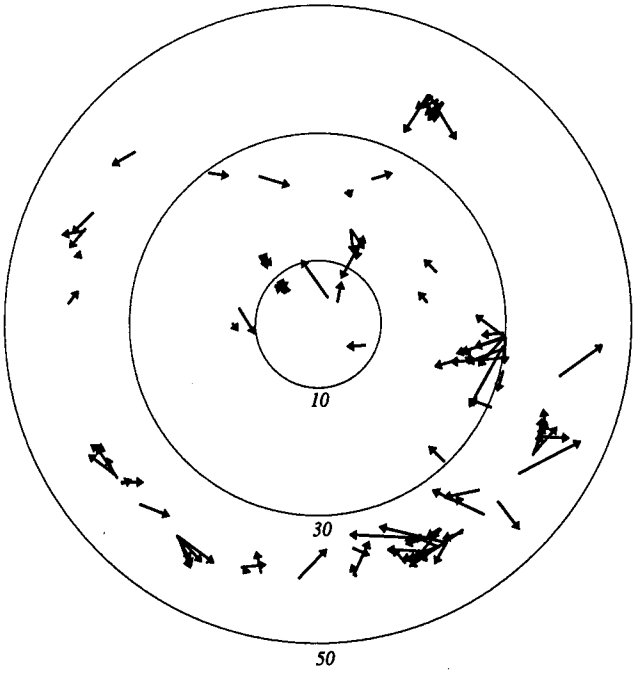

Figure 6. Propagation vector anomalies from array data analysis shown on the lower hemisphere (0°–50°).

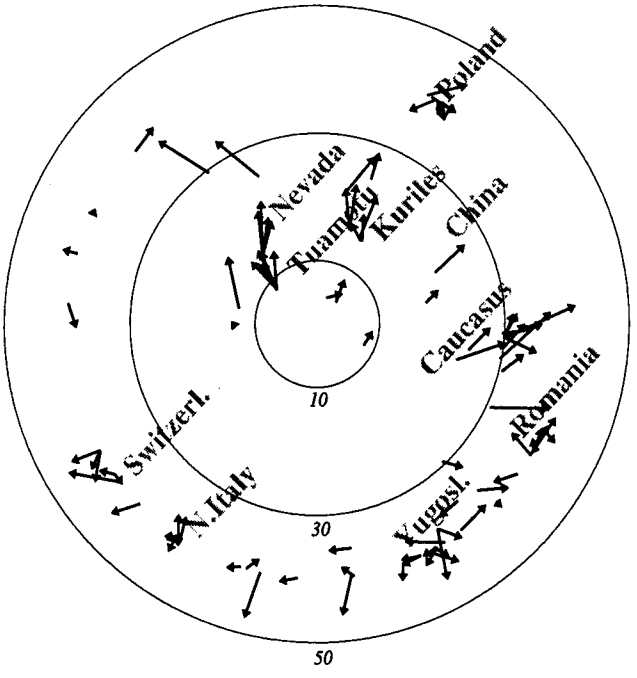

Figure 7. Difference of polarization and propagation vectors shown on the lower hemisphere (0°–50°). These are the data for the inversion procedure in the latter part of this paper.

anisotropy under the receivers. Later on, we use the data of Fig. 7 in an inversion for anisotropy. But first, we briefly review wave-propagation theory in anisotropic media.

3 REVIEW OF PROPAGATION IN ANISOTROPIC MEDIA

Here we wish merely to state features of anisotropic wave propagation which are of particular importance in this study. Comprehensive treatment of the topic has been given, for example, by Crampin (1981). In a general anisotropic medium, the solution for a propagating plane-wave front follows from the Ansatz

$$\mathbf{u}(\mathbf{r}, t) = \mathbf{a}(\mathbf{r}) f(t - \mathbf{n}\mathbf{r}/c), \tag{4}$$

where $\mathbf{a}(\mathbf{r})$ describes amplitude and polarization of the wave, while the time dependence is given by $f()$ depending on the phase velocity c. From the equation of motion, we get

$$m_{il} a_l = c^2 a_i, \tag{5}$$

with the Christoffel matrix

$$m_{il} = c_{ijkl} n_j n_k / \rho. \tag{6}$$

Eq. (6) has the form of an eigenvalue equation with the square of the phase velocity appearing as the eigenvalue. Hence polarization vectors $\mathbf{a}$ serve as eigenvectors. Owing to the symmetry of the elasticity tensor c_{ijkl}, we can always choose a set of three mutually perpendicular eigenvectors. The typical way to solve Eq. (6) is to specify a propagation direction $\mathbf{n}$ and solve for the three eigenvalues and associated eigenvectors. It is clear that in general propagation and polarization vectors do not coincide for waves propagating in anisotropic media. On the other hand, they coincide in the isotropic case. Such deviations can be used to determine effective medium anisotropy. For the case of P waves, we will discuss this discrepancy more closely below, since both of these directions can be observed using arrays and three-component stations.

The wavefront propagates in the normal direction with the phase velocity $c = |\nabla t|^{-1}$. ∇t is the propagation vector, which can be estimated from data of small arrays (see also Helbig 1958). On the other hand, the polarization vector $\mathbf{a}$ gives the direction of local particle motion. It is measured directly by polarization analysis. Neither of these two vectors should be confused with the group velocity vector, which is the direction, in which energy propagates (Musgrave 1970). Crampin, Stephen & McGonigle (1982) showed that for weak anisotropy the differences between polarization and group velocity directions are small. This is intuitively clear, since the energy should propagate in a direction near the particle motion.

While the angular deviation between phase and group velocity vectors received quite some interest in the literature (Crampin 1981; Crampin *et al.* 1982), the relation between phase velocity and polarization vectors has been discussed for model crystals (Crampin 1978, 1981; Crampin *et al.* 1982), but due to a lack of appropriate data, there are only a few applications to real data so far (White *et al.*, 1983; Li, Leary & Aki 1987; de Parscau 1991a). However, deviations of polarization directions from propagation directions can be substantial as will be seen below. In the following we want to illustrate this effect and later on exploit it in an inversion for effective anisotropic structure. It is important to note that the polarization depends only on local anisotropy. This is illustrated in Fig. 8. In the context of anisotropy, P-wave polarizations have been studied for VSP borehole data by de Parscau (1991a) and Li *et al.* (1987). However, with a 1-D array in the borehole, there is no control over off-azimuth arrivals.

We have seen that our method of relative analysis is insensitive against distant heterogeneity. But how about near-receiver heterogeneity? Inspection of polarization hemispheres for individual three-component instruments showed some station-dependent scatter which is partly due to deviations of the instrument response from nominal values. Small-scale heterogeneity near the receivers may

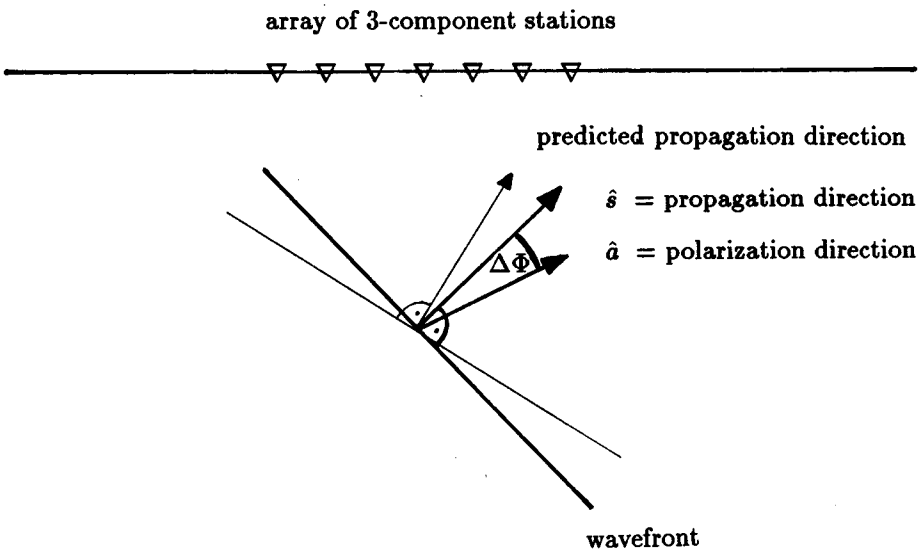

Figure 8. Illustration of plane P-wave propagation in the crust under the three-component receiver array. In an anisotropic medium, the polarization directions generally deviate from the propagation directions. This deviation, here shown for the incidence angle $\Delta\Phi$, is used to infer effective crustal anisotropy. Note that the propagation direction typically deviates from the predicted propagation direction, due to source mislocation and distant heterogeneity. With observations of polarization and propagation directions distant effects can be excluded. Local disturbances of the wavefront are downweighted by averaging over all three-component stations.

also cause waveform distortions. Hence, polarization data from single three-component stations have to be regarded with caution. For our purposes we average over all three-component stations of the array, thereby obtaining average polarization attributes, where array stations are well distributed over an aperture of 4 km. The effect of near-receiver small-scale heterogeneity is expected to be nearly uncorrelated from station to station and we expect the averaging procedure to be effective in averaging out most of its effect on the difference pattern. The effect of larger scale heterogeneity on the other hand, is likely correlated from station to station. We obtain a net effect in the polarization vectors; similarly in the propagation vectors. The difference should therefore again be approximately unaffected. This argument suggests that although scatter is invariably present in difference patterns like Fig. 7, the scatter is dominated by random fluctuation and not by biases from discrete local scatterers. A very important feature of the GERESS array is the absence of a seismologically significant near-surface low-velocity layer, which can be shown from inspection of the train of P–S conversions.

4 UPPER CRUSTAL ANISOTROPY

Anisotropy in the vicinity of the receivers, however, does affect the relative data in Fig. 7. Which depth range are these data sensitive to? We have seen that polarization is a local property. This means that finite-wavelength seismological phases are affected by anisotropy in the depth range equivalent to about a wavelength. For the typical dominant frequencies in this study we have wavelengths of about 6 km. Hence, we expect to estimate a spatial average of anisotropic properties of the top few kilometres in the upper crust. Since we average over all three-component stations in the array, we assume that discrete heterogeneity within the array can be ignored and allow for an anisotropic but homogeneous model.

In this context, there are several phenomena which may cause effective anisotropy. Intrinsic anisotropy of minerals, as well as small-scale structure with some preferred symmetry lead to directional dependence of macroscopic elastic parameters and hence propagation velocity. Sedimentary layering, with a potentially prominent effect, is not present under the array. However, cracks, fractures and rock foliation (Babuska & Cara 1991), if certain orientations prevail, can give rise to substantial effects. Since our data are sensitive to a spatial average over several kilometres, we expect macroscopic anisotropic behaviour either if the anisotropy is locally very strong or if preferred orientation is spatially coherent over a depth range of several kilometres within the topmost part of the upper crust. The latter may, for example, be the case for cracks caused by the regional stress field. Note that our P-wave polarization data are sensitive only to the depth range where brittle deformation is expected.

4.1 General anisotropic model/transversely isotropic case

Since the cause of anisotropy is not known beforehand, it is preferable to find elastic constants without restricting assumptions. In the following we study the type of constraints P-wave polarization data impose on elastic constants. We restrict our attention to the case of hexagonal symmetry, since this is a viable model for most of the possible causes of effective anisotropy mentioned above. An exception may be more complex intrinsic anisotropy of individual crystals, which is not considered here. In the case of a hexagonal or transversely isotropic symmetry, the elastic constant matrix c_{ijkl} has the simple shape

$$c_{ijkl} = \begin{pmatrix} c_{11} & c_{11}-2c_{66} & c_{13} & & & \\ c_{11}-2c_{66} & c_{11} & c_{13} & & & \\ c_{13} & c_{13} & c_{33} & & & \\ & & & c_{44} & & \\ & & & & c_{44} & \\ & & & & & c_{66} \end{pmatrix} \tag{7}$$

with five unknowns, assuming that the symmetry axis is in x_3-direction. Given this particular symmetry, velocity v and polarization direction of P waves depend only on the angle χ between propagation direction and symmetry axis x_3.

4.2 Modelling of *P*-velocity and polarization patterns

White (1983) and de Parscau (1991b) give exact expressions for velocity v and polarization angle ξ

$$\rho v^2 = \tfrac{1}{2}(c_{11}+c_{44})\sin^2\chi + (c_{33}+c_{44})\cos^2\chi + \{[(c_{11}-c_{44})\sin^2\chi - (c_{33}-c_{44})\cos^2\chi]^2 + 4(c_{13}+c_{44})^2\cos^2\chi\sin^2\chi\}^{1/2}, \tag{8}$$

$$\tan\xi = \frac{(c_{13}+c_{44})\cos\chi\sin\chi}{\rho v^2(\chi) - (c_{11}\sin^2\chi + c_{44}\cos^2\chi)}, \tag{9}$$

where ξ is measured from the symmetry axis. Eqs (8) and (9) depend only on the four elastic constants c_{11}, c_{13}, c_{33} and c_{44}. The last constant c_{66} in eq. (7) can be determined only from quasi-transversely polarized shear waves. de Parscau (1991b) showed that (9) can be simplified to

$$\tan 2\xi = \frac{\eta\sin 2\chi}{1-(1+\tau)\sin^2\chi} \tag{10}$$

using the two parameters

$$\eta = \frac{c_{13}+c_{44}}{c_{33}-c_{44}} \tag{11}$$

and

$$\tau = \frac{c_{11}-c_{44}}{c_{33}-c_{44}}. \tag{12}$$

This shows that we will, for example, not be able to determine independently the four elastic constants c_{11}, c_{13}, c_{33} and c_{44} from P-polarization data. Instead, constraints on these constants must be derived from η and τ using the non-linear relations (11) and (12). In addition to η and τ, the orientation of the symmetry axis is unknown. Therefore we have two additional unknowns representing strike and dip of the symmetry axis. Both τ and η can be seen as measures of anisotropy. Since c_{11} and c_{33} give ρv^2 parallel and normal to the symmetry planes, τ gives a measure of the velocity deviation between these special directions. η is

more difficult to interpret, but it can be approximately related to the P-velocity anisotropy at small incidence angles nearly normal to the symmetry planes (de Parscau 1991b). For an isotropic medium we have $\eta = \tau = 1$.

A number of criteria on the elastic coefficients in eq. (7) can be derived from requiring stability, namely the condition that deformation is associated with non-negative internal energy. The requirement is that (7) is positive semi-definite (Backus 1962). It follows that all diagonal elements are non-negative. Furthermore we have $c_{11} \geq c_{66}$ and $c_{33}(c_{11} - c_{66}) \geq c_{13}^2$. In our context, bounds on elastic coefficients are important for finding bounds on the parameters η and τ and for rejecting physically impossible models. Postma's (1955) inequality

$$(c_{11} - c_{44})(c_{33} - c_{44}) \geq (c_{13} + c_{44})^2 \tag{13}$$

shows that $\tau \geq 0$. Since τ gives a measure of the size of P-wave anisotropy, an upper bound may be given from an estimate of maximum possible anisotropy. The sign of $c_{13} + c_{44}$, which is the nominator of η, is found to have substantial importance for the polarization behaviour. Cases with $c_{13} + c_{14} \leq 0$ are physically possible, but they are found only in very carefully planned laboratory experiments (Helbig & Schoenberg 1988). In these cases, the polarization angle is found to rotate in a sense opposite to the propagation direction, in contrast to the normal case with rotation in the same sense. For real Earth studies it is reasonable to assume $c_{13} + c_{44} \geq 0$, which gives us a lower bound $\eta \geq 0$. An upper bound on η can be found by applying a requirement that c_{11}/c_{44} and c_{33}/c_{44} be within a certain range.

Now we illustrate polarization behaviour for two special cases, namely $(\eta, \tau) = (1.43, 2.13)$ and $(0.82, 1.00)$. These cases correspond to elastic parameters for models HCD1 and HCS1 (Crampin 1984), which give the effective anisotropy associated with a model of oriented cracks (Hudson 1981) in the limiting cases of fluid-saturated and dry conditions. To derive this model of oriented cracks, Hudson (1980) used mean field theory (Keller 1964) and derived expressions valid to second order. In his perturbative treatment the stiffness matrix can be represented as

$$c_{ijkl} = c^0_{ijkl} + c^1_{ijkl} + c^2_{ijkl} \tag{14}$$

for long wavelengths, where the zero-order term gives the isotropic reference model specified by the Lamé parameters λ and μ

$$c^0_{ijkl} = \lambda \delta_{ij}\delta_{kl} + \mu(\delta_{ik}\delta_{jl} + \delta_{il}\delta_{jk}). \tag{15}$$

The first- and second-order perturbation terms can be interpreted as a first-order effect of the cracks and crack–crack interaction. For the crack density $\epsilon = Na^3/V$ (N/V = number of cracks per volume, a = mean crack radius) they are

$$c^1_{ijkl} = -\frac{\epsilon}{\mu} \begin{pmatrix} \lambda^2 & \lambda^2 & \lambda(\lambda+2\mu) & & & \\ \lambda^2 & \lambda^2 & \lambda(\lambda+2\mu) & & & \\ \lambda(\lambda+2\mu) & \lambda(\lambda+2\mu) & (\lambda+2\mu)^2 & & & \\ & & & \mu^2 & & \\ & & & & \mu^2 & \\ & & & & & 0 \end{pmatrix} \mathbf{D} \tag{16}$$

and

$$c^2_{ijkl} = \frac{\epsilon^2}{15} \begin{pmatrix} \lambda^2 q/(\lambda+2\mu) & \lambda^2 q/(\lambda+2\mu) & \lambda q & & & \\ \lambda^2 q/(\lambda+2\mu) & \lambda^2 q/(\lambda+2\mu) & \lambda q & & & \\ \lambda q & \lambda q & (\lambda+2\mu)q & & & \\ & & & x & & \\ & & & & x & \\ & & & & & 0 \end{pmatrix} \mathbf{D}^2 \tag{17}$$

with $q = 15(\lambda/\mu)^2 + 28(\lambda/\mu) + 28$ and $x = 2\mu(3\lambda + 8\mu)/(\lambda + 2\mu)$. Here the cracks are aligned perpendicular to x_3. $\mathbf{D}$ is the diagonal matrix with trace

$$\text{trace}\,(\mathbf{D}) = (u_{11}, u_{11}, u_{11}, u_{33}, u_{33}, 0). \tag{18}$$

u_{km} depends on conditions on the crack face. The dependence of c_{ijkl} on the crack parameters is only through $\mathbf{D}$ and is further given by

$$u_{11} = \frac{4}{3}\frac{(\lambda+2\mu)}{(\lambda+\mu)} \Big/ (1+k) \tag{19}$$

and

$$u_{33} = \frac{16}{3}\frac{(\lambda+2\mu)}{(3\lambda+4\mu)} \Big/ (1+m) \tag{20}$$

with k and m given as

$$k = \left(\frac{\lambda'+2\mu'}{\pi d\mu}\right) \Big/ \frac{(\lambda+2\mu)}{(\lambda+\mu)} \tag{21}$$

and

$$m = \frac{4\mu'}{\pi d\mu}\frac{(\lambda+2\mu)}{(3\lambda+4\mu)}. \tag{22}$$

The ϵ range of interest in this study is between 0 and 0.1. For such low values of ϵ, the second-order approximation is considered uncritical (Crampin 1981). d gives the (large) aspect ratio of the cracks and λ' and μ' are the Lamé parameters within the cracks. The two extreme cases with particular physical significance are (1) $\mu' = \lambda' = 0$ and (2) $\mu' = 0$ with non-zero λ'.

The first case models dry cracks (HCD1), with free surfaces at the crack faces. In this case k and m vanish. The polarization pattern is determined solely by the two parameters $(\eta, \tau) = (1.43, 2.13)$. P-wave phase velocities and polarizations for this model of vertical east-west oriented cracks are shown in Fig. 9 in lower hemisphere representations, where for display purposes the symmetry axis is shown pointing upwards in the paper plane. We choose the unconstrained absolute levels of c_{11}, c_{44} and c_{66} to conform to model HCD1 (background velocity $v_P = 5.8\ \text{km s}^{-1}$, $v_S = 3.349\ \text{km s}^{-1}$, density $\rho = 2.6\ \text{km s}^{-1}$).

This choice affects only the P-velocity pattern, but not the polarization pattern, which depends only on η and τ. Propagation in the plane of aligned cracks gives high velocity and the P-wave anisotropy for this ideal model is 24 per cent. The right-hand side shows polarization anomalies, namely deviations of the polarization from propagation directions. In general, the polarization direction deviates to the direction of larger phase velocity, diverging at the symmetry axis and converging to the symmetry plane.

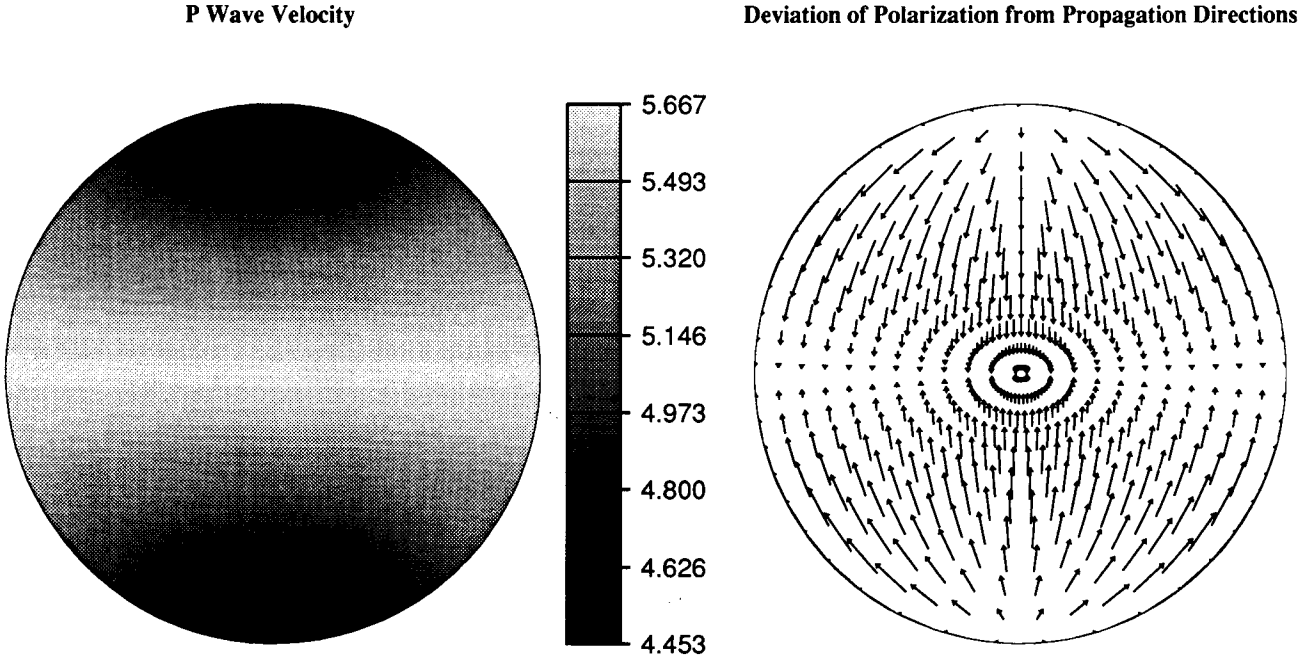

Figure 9. Lower hemisphere representation of P-wave velocity and polarization anomalies for $(\eta, \tau) = (1.43, 2.13)$ corresponding to the dry-crack model HCD1 of Crampin (1984).

For the second case (model HCS1), which models saturated cracks, we obtain Fig. 10. The parameters are the same as in Fig. 9, but with aspect ratio $d = 0.0001$ and $\lambda' = 2.25$ GPa. The polarization pattern is then given by $\eta = 0.82$ and $\tau = 1$. Note that this velocity pattern differs substantially from the dry-crack model: the symmetry axis also has fast velocity. This gives rise to $\tau = 1$. Clearly, τ is very sensitive in distinguishing dry-crack conditions from saturated ones. The difference between minimum and maximum velocity with 3.5 per cent anisotropy is substantially smaller than for the dry-crack model. The maximum velocity achieved is somewhat higher than for the dry-crack model though. Polarization anomalies are smaller but give a more complex pattern.

5 MODEL FITTING

Observed polarization anomalies can be related to the parameters η and τ describing the anisotropy. The inverse problem requires the solution of the eigenvalue problem (6).

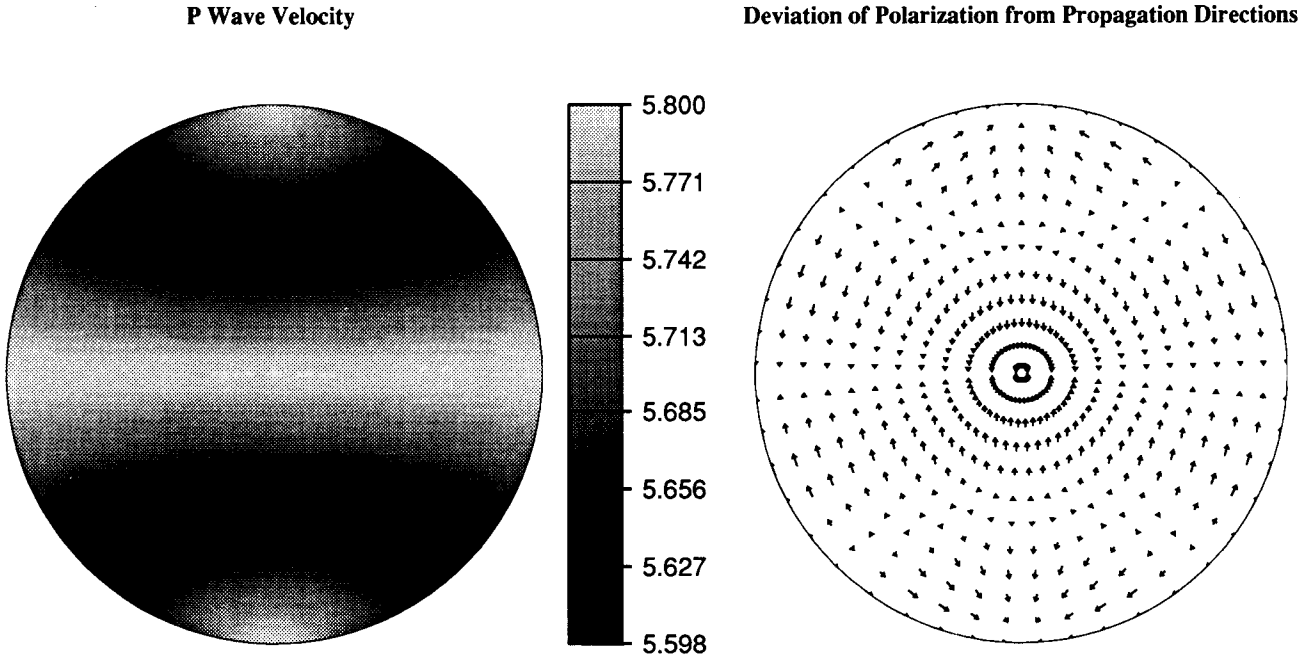

Figure 10. Lower hemisphere representation of P-wave velocity and polarization anomalies for $(\eta, \tau) = (0.82, 1.00)$ corresponding to the saturated-crack model HCS1 of Crampin (1984).

In this paper, this is done by non-linear parameter fitting. As shown above, parameters in the inversion are η and τ, but also two angles $\tilde{\theta}$ and $\tilde{\Phi}$ describing azimuth and dip of the symmetry axis. In general, we will not be able to determine the four elastic constants independently. Instead we may obtain two non-linear constraints on these parameters from η and τ, which we may supplement with *a priori* information. In our case, such information is given by reasonable assumptions about the reference velocity. In the following we use reference velocities of the above examples HCD1 and HCS1. This enables us to display velocity patterns for the inversion results also.

For each event we have an observation of polarization direction (θ_a ϕ_a) and propagation direction (θ_s ϕ_s). We wish to compare the angular differences

$$\begin{pmatrix}\Delta\theta\\ \Delta\phi\end{pmatrix}=\begin{pmatrix}\theta_a-\theta_s\\ \phi_a-\phi_s\end{pmatrix}$$

with predictions from models depending on the parameters ($\tilde{\theta}$, $\tilde{\Phi}$, η, τ), which we call

$$\begin{bmatrix}\Delta\theta_i'(\eta,\tau,\tilde{\theta},\tilde{\phi}\\ \Delta\phi_i'(\eta,\tau,\tilde{\theta},\tilde{\phi}\end{bmatrix}$$

for the ith event. We obtain the best-fitting model by inspecting the misfit on the sphere

$$S(\tilde{\theta},\tilde{\Phi},\eta,\tau)=\frac{1}{N}\sum_{i=1}^{N}\{\cos^{-1}\times[\cos(\Delta\theta_i-\Delta\theta_i')\cos(\Delta\phi_i-\Delta\phi_i')]\}^2, \quad (23)$$

which is the analogue of the standard sum-of-squares misfit criterion on the sphere.

The models HCD1 and HCS1 have shown that the polarization pattern may vary considerably, depending on the choice of η and τ. We start the discussion of inversion results by studying the dependence of the misfit on symmetry axis orientation for these two special cases. η and τ are fixed to (1.43, 2.13) in the first case of dry cracks and (0.82, 1.) in the case of saturated cracks. We are left with fitting $\tilde{\theta}$, and $\tilde{\Phi}$. The non-linear search may use a rotation of the elastic constant matrix

$$c_{ijkl}=\tau_{ip}\tau_{jq}\tau_{kr}\tau_{ls}c_{pqrs} \quad (24)$$

with the rotation matrix τ. While this allows for all types of symmetry, we may more efficiently use eq. (9) in our case of hexagonal symmetry. Results for the dry-crack case are given in Fig. 11 showing the achieved misfit S given in degree^2 by eq. (23) depending on the orientation of the symmetry axis, namely its location in the lower hemisphere. Axes orientations with small misfit are near the circumference. The smallest achieved misfit is 135 degree^2, which is substantially larger than the starting misfit of 68.87 degree^2. The simple dry-crack model is clearly incompatible with the data. On the other hand, the saturated-crack model (Fig. 12) gives reasonable variance reduction of about 41 per cent. Fig. 12(a) shows that small misfits are achieved for symmetry axis locations in two regions in the south-west and north-east. Only the south-western region gives rise to statistically significant solutions. The lowest contour shows the confidence region where the critical misfit level is computed from the f-distribution as

$$S_{\text{crit}}=S_{\text{opt}}\left[1+\frac{k}{N-k}f_{k,N-k}(1-\alpha)\right] \quad (25)$$

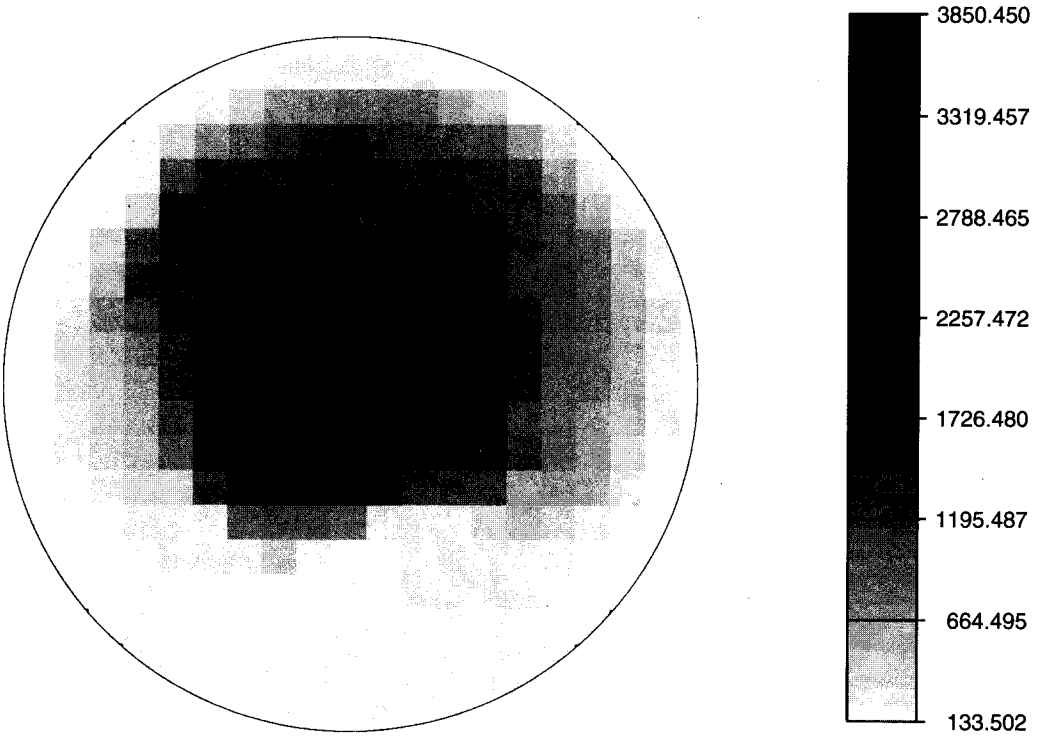

Figure 11. Fitting of the dry-crack model. Misfit on the sphere (23) is shown in degree^2, depending on the symmetry axis orientation. Smaller misfits are found for axes located near the horizontal plane. This dry-crack model does not improve the misfit and hence cannot explain the data.

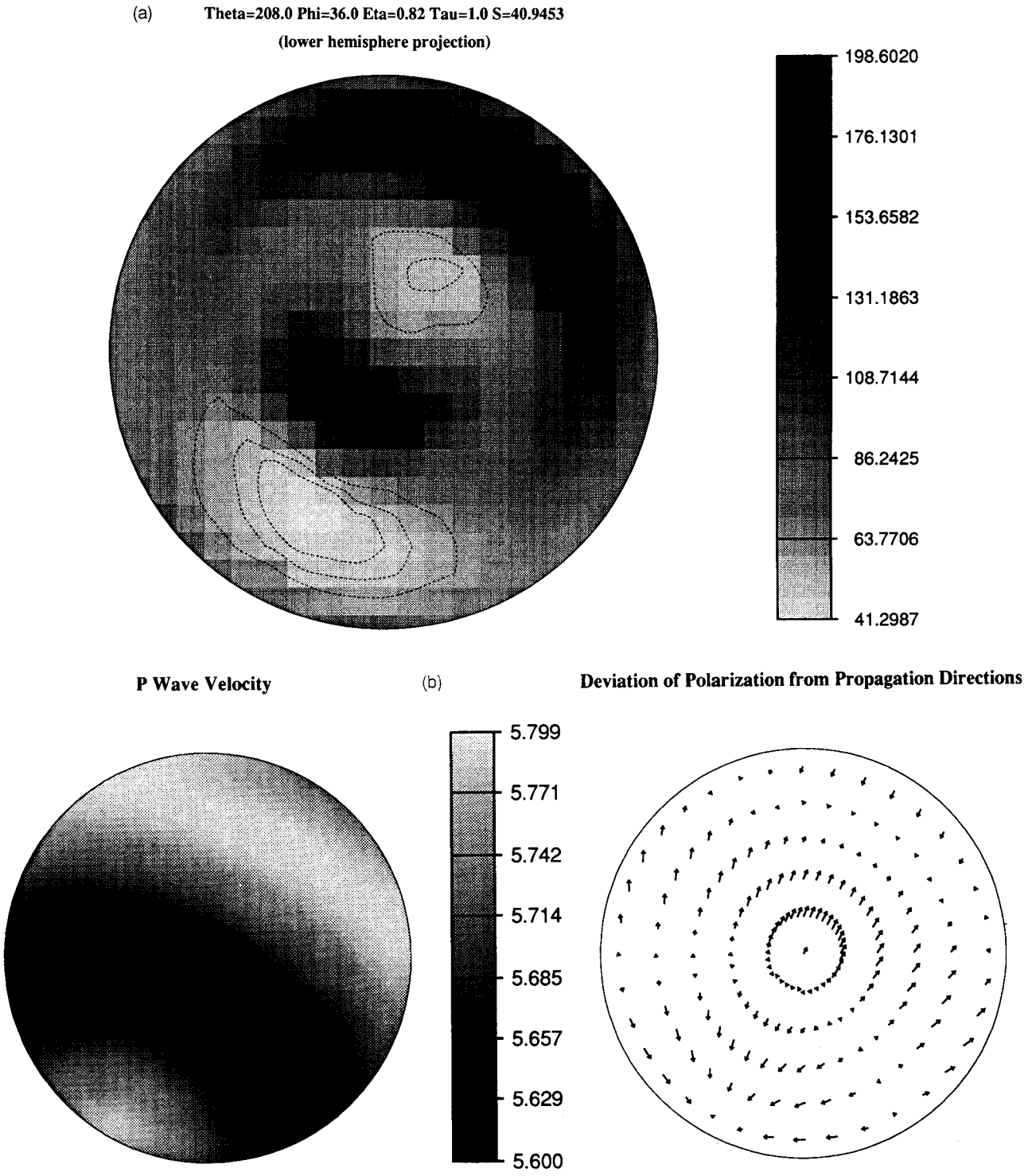

Figure 12. Fitting of the saturated-crack model: (a) misfit in degree^2 depending on symmetry axis orientation from 0° to 90° incidence; (b) best-fitting model shown in a partial lower hemisphere display (0°–55° incidence). The symmetry axis has a strike of 208° and a dip of 36° to the south. The lowest contour line gives the critical level. Polarization deviations are given for 0°, 10°, . . . , 50° incidence.

(Jenkins & Watts 1969), where S_{opt} is the minimum misfit and $k = 4$ the number of parameters. Higher contours give two and four times the separation of the critical level ($1 - \alpha = 0.95$ per cent confidence level) from the minimum level. The optimum model has a symmetry axis orientation of azimuth $\bar{\theta} = 208°$ and dip $\bar{\Phi} = 36°$. The symmetry plane is oriented normal to the symmetry axis, and has strike 118° and dip 54° to the north. The optimum model corresponding to the global minimum in the south-west is shown in Fig. 12(b) by its velocity and polarization pattern. To be directly comparable with the data, only the partial lower hemisphere from 0° to 55° is shown. Beside the symmetry plane, also the symmetry axis shows up with fast velocity in the lower part of the figure. The polarization deviations in the right-hand

side of Fig. 12b are given for 0°, 10°, . . . , 50° incidence and may be compared with the data in Fig. 7. The major features of the data set are explained by the model.

The results for assumed dry- and saturated-crack models are quite different. The saturated-crack model gave a reasonable fit to the data and a strike angle of the high-velocity plane of 118°, while the dry-crack model was in clear conflict with the data.

Now we perform the more general non-linear search for the parameter set $(\tilde{\theta}, \tilde{\Phi}, \eta, \tau)$, which unlike the previous example does not assume a particular physical fracture model. With four parameters and the given bounds on η and τ this search is not particularly computer intensive, but guarantees the globally optimal solution, given that the bounds are appropriate and the sampling is sufficiently fine. The misfit pattern in Fig. 13(a) is not unlike the one for the saturated-crack model. However, the optimum in the south-west is more pronounced now and the variance

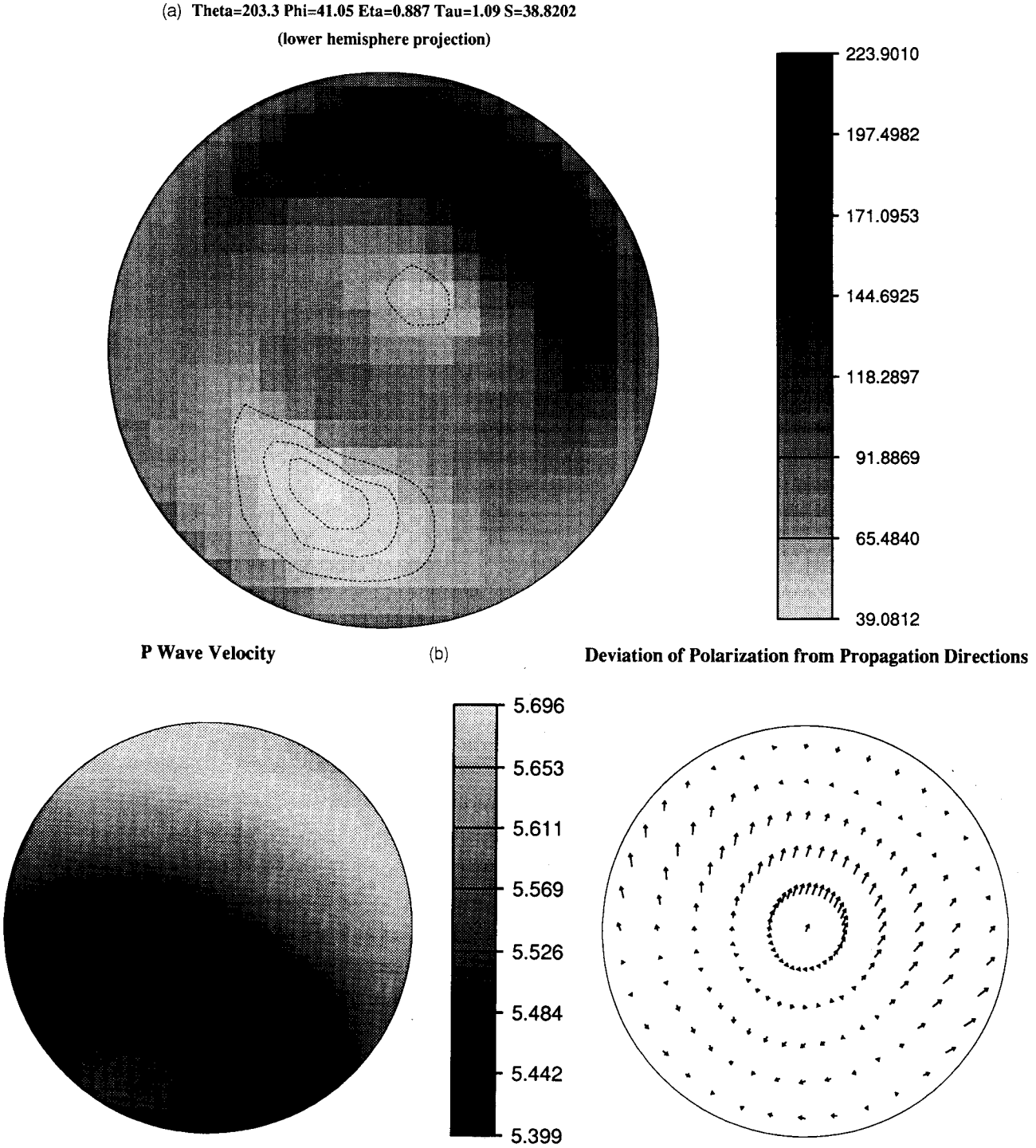

Figure 13. Result of the general non-linear search: (a) misfit (0°–90° incidence); (b) optimum model in the partial lower hemisphere display (0°–55°). With the symmetry axis at 203.3° and 41.05°, the (high-velocity) symmetry plane has a strike of about 113° and dips of about 58° to the north. The optimum set of parameters is $\eta = 0.887$ and $\tau = 1.09$.

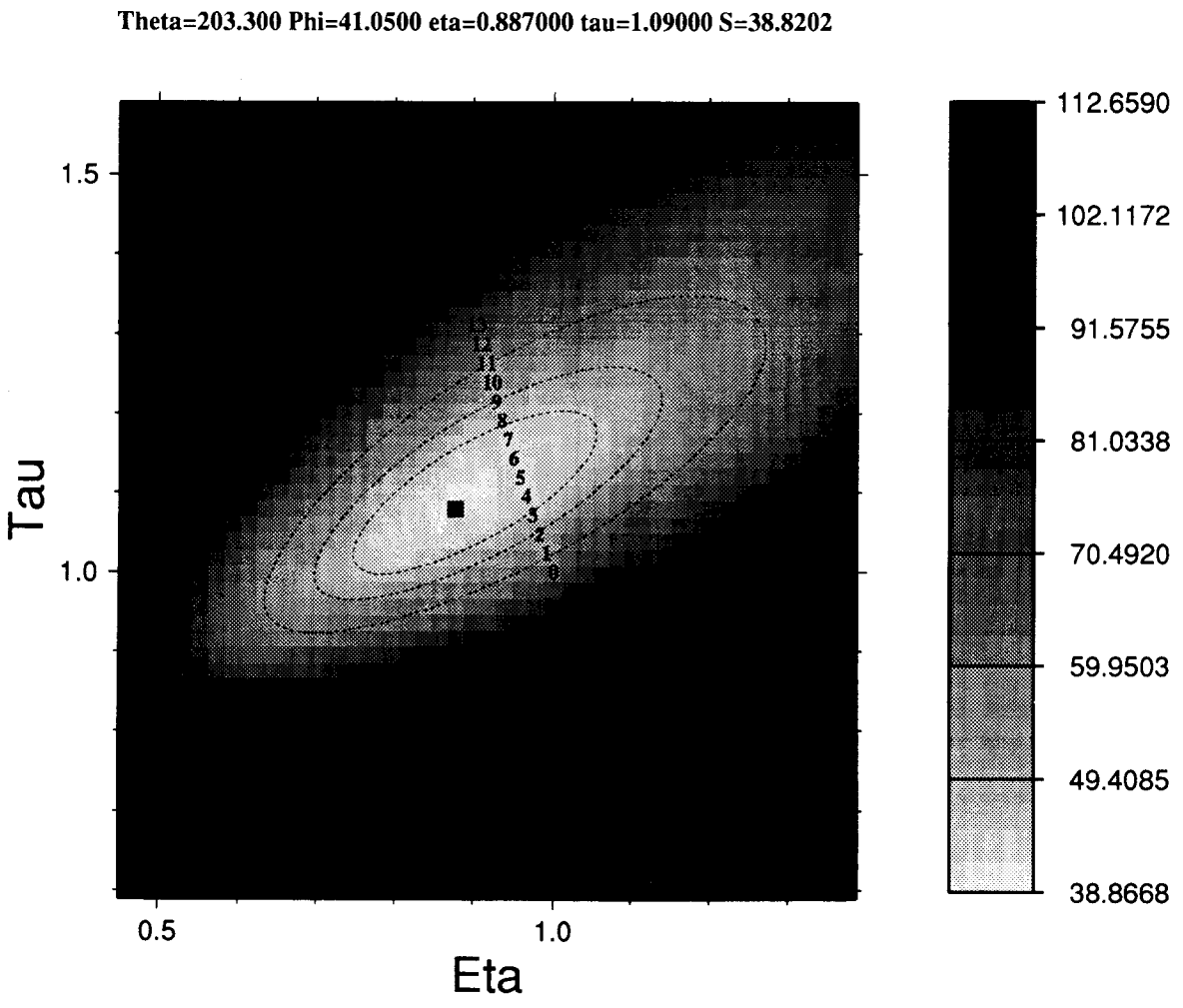

Figure 14. Misfit around the optimum model (black square) keeping the orientation fixed. The lowest contour line shows the confidence region around the best-fitting model. Numbers 0–13 refer to percentages of mica content in a gneiss model (see test).

reduction is 3 per cent larger, now about 44 per cent. The resulting parameters are $\bar{\theta} = 203.3°$, $\bar{\Phi} = 41.05°$, $\eta = 0.887$ and $\tau = 1.09$. The maximum P-velocity difference of the model is about 4.7 per cent. The change in orientation from the fit of model HCS1 by a few degrees is insignificant considering the large confidence region in Fig. 12(a). In the general model, the confidence region is substantially smaller. For the polarizations, the main difference is the behaviour in the south-western part, where the general model predicts a somewhat smaller effect. This corresponds to the smaller velocity contrast in that region. The high-velocity symmetry plane strikes with about 113° and dips with about 49° to the north-east.

In the search we varied η and τ independently. But can they be resolved independently by the data constraints or are they subject to a major trade-off? Fig. 14 shows the misfit around the optimum model keeping the symmetry axis orientation fixed and varying η and τ. The lowest contour again shows the confidence region of admissible η and τ, which extends for η from 0.76 to 1.07 and for τ from 1 to 1.2. The isotropic case at $\eta = 1$ and $\tau = 1$ is well outside the highest contour for four times the critical misfit separation.

6 WHAT CAUSES THE EFFECTIVE ANISOTROPY?

In principle, intrinsic anisotropy as well as macroscopic effects from oriented cracks, fractures or layering can cause anisotropy of this size. To understand the nature of this anisotropy, it is of considerable value to also consider surface geological evidence for the region. The array is located on an outcrop of granite and gneiss. While the granite apparently has no preferred alignment, the gneiss shows strong foliation with consistent orientations. The strike is approximately 120° and the dip 50°–60° (Ott, private communication). This closely coincides with the orientation of the high-velocity planes for the best-fitting model from the unconstrained inversion (Fig. 13) suggesting that rock foliation is the major cause of anisotropy in this case. The size of the anisotropy suggests that the foliation direction is spatially consistent over some distance, perhaps several kilometres. In fact, surface geology does suggest that this is indeed the case (Ott, private communication). Rock foliation as a cause of effective anisotropy has been discussed before (e.g. Lüschen *et al.* 1991).

But is rock foliation the only factor involved and how does the overall anisotropy relate to intrinsic properties of minerals? Gneisses typically contain large amounts of mica, a mineral giving rise to very large anisotropy. Since this mineral is usually quite well oriented (Wang, Lin & Wenk 1975), we may expect a major effect on the observed anisotropy. In fact, mica orientations are typically dominant in forming macroscopic gneiss foliation planes (Suppe 1985). Pure mica, however, does not explain the observed effect: Aleksandrov & Ryzhova (1961) give elastic constants for muscovite, for which we compute $\eta = 0.625$ and $\tau = 3.88$. The latter value is clearly incompatible with our results. More realistic models would include structural complexity, the occurrence of several types of intrinsic anisotropy, and fractures or cracks in the subsurface. In fact, we have physical models at our disposition predicting some of these effects. For a medium consisting of anisotropic layers, Schoenberg & Douma (1988) give expressions for averaging elastic constants to obtain effective elastic constants in the long-wavelength assumption. Also, for such a medium, effective parameters $\bar{\eta}$ and $\bar{\tau}$ are composed of the averaged elastic constants as

$$\bar{\eta} = \frac{\bar{c}_{13} + \bar{c}_{44}}{\bar{c}_{33} - \bar{c}_{44}}, \tag{26}$$

$$\bar{\tau} = \frac{\bar{c}_{11} - \bar{c}_{44}}{\bar{c}_{34} - \bar{c}_{44}}, \tag{27}$$

using

$$\bar{c}_{11} = \langle c_{11} \rangle - \langle c_{13}^2 / c_{33} \rangle + \langle c_{13}/c_{33} \rangle^2 / \langle 1/c_{33} \rangle, \tag{28}$$

$$\bar{c}_{13} = \langle c_{13}/c_{33} \rangle / \langle 1/c_{33} \rangle, \tag{29}$$

$$\bar{c}_{33} = 1/\langle 1/c_{33} \rangle, \tag{30}$$

$$\bar{c}_{44} = 1/\langle 1/c_{44} \rangle, \tag{31}$$

where $\langle\rangle$ denotes the thickness-weighted average of the respective quantity. If we take the simple approach of assuming that due to their large effect only micas contribute to the bulk anisotropy, we may simply compute η and τ for different percentages of mica content. For a fraction of 30 per cent mica after Wang *et al.* (1975) and 70 per cent other material assumed to be isotropic we obtain $\eta = 0.816$ and $\tau = 1.74$. While this is far outside the confidence region of the observation, values for 3–8 per cent mica content fall within the confidence region (Fig. 14). These are low values compared with mica contents in typical gneisses (Wang *et al.* 1975). We have to keep in mind though that certainly not all of the mica minerals are fully aligned. Other constituents may also play a role in defining the bulk anisotropy.

Satisfying the polarization data, this gneiss model is also a plausible explanation in conjunction with the geological data. Another possible model, however, is that of cracks or fractures aligned in the direction of planes of weakness which coincide with the gneiss foliation. Fitting a model of aligned cracks after Hudson (1981) gave essentially the same orientation. Resulting parameters were strike 114° and dip 50° for the symmetry planes. We also obtained a crack density of $\epsilon = 0.09$ and two Lamé parameters of the crack material $\lambda' = 0.049$ GPa and $\mu' = 0$ GPa. The associated error bars discriminate clearly against the dry-crack case, where $\lambda' = 0$ GPa. Such dry cracks give rise to large values of τ, which we have previously argued, are in conflict with the data. Based on the achieved misfit, the model of cracks opening along the foliation planes can not be ruled out.

It appears difficult to distinguish between models of intrinsic anisotropy and cracks or fractures. In this case, one should consider all possible models. In fact, the occurrence of cracks along planes of weakness given by foliation planes is not unlikely. For small pressures in the laboratory, it is very common to observe cracks opening along the foliation direction. This can be demonstrated, for example, with the data of Wang *et al.* (1975). From their data we obtain values of $\tau \approx 1.25$ at 1 kbar pressure and much larger values up to 10 at lower pressure. Crack opening can be caused by the

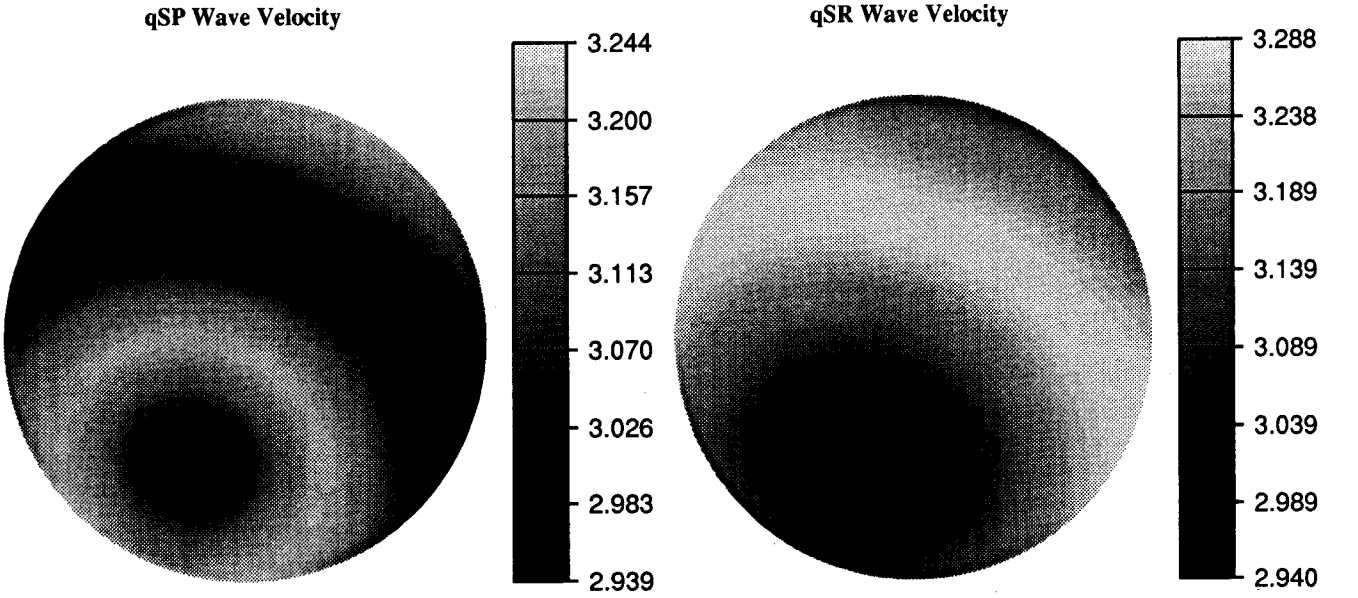

Figure 15. Prediction of shear-wave velocities for the optimum model on the full lower hemisphere (0°–90°). qSP is polarized parallel to the symmetry plane and qSR perpendicular.

local stress field. Values for the strike of the maximum horizontal stress direction σ_H in the area are around 149° in the KTB borehole (Brudy, Fuchs & Zoback 1993), but there are also values in the range of 115° (e.g. Falkenberg granite, Rummel, Baumgärtner & Alheid 1983). These values are not far from the foliation strike. Hence crack opening along the foliation direction is not unlikely, particularly if the fluid pressure is high. However, we note that anisotropy in our data set appears to be due to foliation rather than to vertical cracks perpendicular to the smallest horizontal stress direction. On the other hand, the regional stress field may have an effect due to opening of cracks preferentially parallel to the planes of weakness, which are given by the gneiss foliation planes.

Perhaps additional insight can be gained if shear waves are used. Fig. 15 gives a prediction of the shear-wave velocities for the optimum model. However, unambiguous determination of upper crustal anisotropy requires incidence angles within the shear-wave window and sources close enough to the receivers to not be sensitive to more distant anisotropy. These conditions are difficult to meet for our region. In contrast, *P*-wave polarization data from all types of local, regional and teleseismic events may be used for the study of local anisotropy.

ACKNOWLEDGMENTS

The work of the GERESS group at Bochum is acknowledged, which is supported by ARPA grant AFOSR-90-0189. We thank Hans-Peter Harjes, Bernd Stöckhert, Wolf-Dietrich Ott, Fritz Rummel and Jan Wüster for valuable discussions and Wolfgang Rabbel and an anonymous reviewer for constructive and helpful comments. We also thank Stefan Sauerländer for help in data processing and Paul Wessel and Walter Smith for permission to use the GMT plotting package.

REFERENCES

Aki, K. & Richards, P.G., 1983. *Quantitative Seismology, Theory and Methods,* Vol. I, Freeman, San Francisco.

Aleksandrov, K.S. & Ryzhova, T.V., 1961. The elastic properties of rock-forming minerals, II: layered silicates, *Izv. Acad. Sci. USSR, Geophys. Ser.*, **2.** 186–189.

Ando, M., Ishikawa, Y. & Yamazaki, F., 1983. Shear wave polarization anisotropy in he upper mantle beneath Honshu, Japan, *J. geophys. Res.*, **88** (B7), 5850–5864.

Babuska, V. & Cara, M., 1991. *Seismic Anisotropy in the Earth,* Kluwer Academic Publishers, Dordrecht.

Backus, G.E., 1962. Long-wave elastic anisotropy produced by horizontal layering, *J. geophys. Res.*, **67** (11), 4427–4440.

Backus, G.E., 1965. Possible forms of seismic anisotropy of the uppermost mantle under oceans, *J. geophys. Res.*, **70** (14), 3429–3439.

Beauchamp, K.G., (ed.), 1975. *Exploitation of Seismograph Networks,* Proc. Nato Advanced Study Institute, Sandefjord, Norway, Noordhoff, Leiden.

Bokelmann, G.H.R., 1992. Upper and lower mantle small-scale heterogeneity studied by systematic analysis of portable broadband waveforms and traveltimes, *PhD thesis,* Princeton University, Princeton, NJ.

Bokelmann, G.H.R., 1993. Azimuth and slowness deviations from the GERESS regional array, *Bull. seism. Soc. Am.*, submitted.

Brudy, M., Fuchs, K. & Zoback, M. D., 1993. Stress orientation profile to 6 km depth in the KTB main borehole, in *KTB Rep. 93-2,* pp. 195–197, eds Emmermann, R., Lauterjung, J. & Umsoust, T., Verlagsbuchhandlung, Stuttgart.

Crampin, S., 1978. Seismic-wave propagation through a cracked solid: polarization as a possible dilatancy diagnostic, *Geophys. J. R. astr. Soc.* **53,** 467–496.

Crampin, S., 1981. A review of wave motion in anisotropic and cracked elastic-media, *Wave Motion,* **3,** 343–391.

Crampin, S., 1984. Effective anisotropic elastic constants for wave propagation through cracked solids, *Geophys. J. R. astr. Soc.,* **76,** 135–145.

Crampin, S., Stephen, R. A. & McGonigle, R., 1982. The polarization of *P*-waves in anisotropic media, *Geophys. J. R. astr. Soc.,* **68,** 477–485.

de Parscau, J., 1991a. *P*- and *SV*-wave transversely isotropic phase velocities analysis from VSP data, *Geophys. J. Int.,* **107,** 629–638.

de Parscau, J., 1991b. Relationship between phase velocities and polarization in transversely isotropic media, *Geophysics,* **56**(10), 1578–1583.

Dziewonski, A.M. & Anderson, D.L., 1983. Traveltimes and station corrections for *P* waves at teleseismic distances, *J. geophys. Res.,* **88,** 3295–3314.

Harjes, H.P. 1990. Design and siting of a new regional array in central Europe, *Bull. seism. Soc. Am.,* **80**(B), 1801–1817.

Harjes, H.P., Jost, M.L., Schweitzer, J. & Gestermann, N., 1993. Automatic seismogram analysis at GERESS, *Comput. Geosci.,* **19**(2), 157–166.

Helbig, K., 1958. Elastische Wellen in anisotropen Medien, *Gerlands Beitr. Geophys.,* **67,** 177–211.

Helbig, K. & Schoenberg, M., 1988. Anomalous polarization of elastic waves in transversely isotropic media, *J. acoust. Soc. Am.* **81,** 1235–1245.

Hess, H., 1964. Seismic anisotropy under the uppermost mantle under oceans, *Nature,* **203,** 629–631.

Hudson, J.A., 1980. Overall properties of a cracked solid, *Math. Proc. Camb. Phil. Soc.,* **88,** 371–384.

Hudson, J.A., 1981. Wave speeds and attenuation of elastic waves in material containing cracks, *Geophys. J. R. astr. Soc.,* **64,** 133–150.

Jenkins, G.M. & Watts, D.G., 1969. *Spectral Analysis and its Applications,* Holden-Day, San Francisco.

Jurkewicz, A., 1988. Polarization analysis of three-component array data, *Bull. seism. Soc. Am.,* **78**(5), 1725–1743.

Kanasewich, E.R., 1981. *Time Sequence Analysis in Geophysics,* University of Alberta Press, Edmonton.

Keller, J.B., 1964. Stochastic equations and wave propagation in random media, *Proc. Symp. appl. Math.,* **16,** 145–170.

Li. Y.-G., Leary, P.C. & Aki, K., 1987. Observation and modeling of fault-zone fracture seismic anisotropy—II. *P*-wave polarization anomalies, *Geophys. J. R. astr. Soc.,* **91,** 485–492.

Lüschen, E., Söllner, W., Hohradt, A. & Rabbel, W., 1991. Integrated *P*- and *S*-wave borehole experiments at the KTB-deep drilling site in the Oberpfalz area, in Meissner, R., Brown, L., Dürbaum, H.J., Franke, W. & Seifert, F., American Geophysical Union, Washington, DC. *Continental Lithosphere: Deep Seismic Reflections,* Am. geophys. Un., Geodyn. Ser. 22, pp. 121–133, eds.

Musgrave, M.J.P., 1970. *Crystal Acoustics,* Holden-Day, San Francisco.

Postma, G.W., 1955. Wave propagation in a stratified medium, hydraulic fracturing. *Geophysics,* **20,** 780–806.

Rummel, F., Baumgärtner, J. & Alheid, H.J., 1983. Stress measurements along the eastern boundary of the SW-German block, in *Hydraulic Fracturing Stress Measurements,* pp. 3–17, Zoback, M, L. & Haimson, B. C., National Academic Press, Washington, DC.

Schoenberg, M. & Douma, J., 1988. Elastic wave propagation in

media with parallel fractures and aligned cracks, *Geophys. Prospect.*, **36,** 571–590.

Silver, P.G. & Chan, W. W., 1991. Shear wave splitting and subcontinental mantle deformation, *J. geophys. Res.*, **96**(B10), 16 429–16 454.

Suppe, J., 1985. *Principles of Structural Geology,* Prentice-Hall, Englewood Cliffs, NJ.

Wang, C.-Y., Lin, W. & Wenk, H.-R., 1975. The effects of water and pressure on velocities of elastic waves in a foliated rock, *J. geophys. Res.* **80,** 1065–1069.

White, J.E., 1983. *Underground Sound, Application of Seismic Waves,* Elsevier, Amsterdam.

White, J.E., Martineau-Nicoletis, L. & Monash, C., 1983. Measured anisotropy in Pierre Shale, *Geophys. Prospect.*, **31,** 709–725.